Published in final edited form as:

IEEE Trans Antennas Propag. 2017 May ; 65(5): 2624–2634. doi:10.1109/TAP.2017.2677398.

Ray Tracing and Modal Methods for Modeling Radio Propagation in Tunnels With Rough Walls

Chenming Zhou [Member, IEEE]

Office of Mine Safety and Health Research, National Institute for Occupational Safety and Health, Pittsburgh, PA 15236 USA

Abstract

At the ultrahigh frequencies common to portable radios, tunnels such as mine entries are often modeled by hollow dielectric waveguides. The roughness condition of the tunnel walls has an influence on radio propagation, and therefore should be taken into account when an accurate power prediction is needed. This paper investigates how wall roughness affects radio propagation in tunnels, and presents a unified ray tracing and modal method for modeling radio propagation in tunnels with rough walls. First, general analytical formulas for modeling the influence of the wall roughness are derived, based on the modal method and the ray tracing method, respectively. Second, the equivalence of the ray tracing and modal methods in the presence of wall roughnesses is mathematically proved, by showing that the ray tracing-based analytical formula can converge to the modal-based formula through the Poisson summation formula. The derivation and findings are verified by simulation results based on ray tracing and modal methods.

Index Terms

Tunnel propagation; ray tracing; waveguide theory

I. Introduction

Radio propagation in tunnels has been investigated for decades [1]–[8], partially driven by the need for communication among underground miners. Although many methods have been developed, ray tracing and modal methods are the two major analytical approaches for modeling radio propagation in straight tunnels.

The ray tracing method treats radio waves as ray tubes, and the electrical field at any location within a tunnel is represented by a summation of the rays reaching the location [9]. The modal method, on the other hand, assumes that waves propagate in the form of modes and the electrical field is represented in terms of a summation of modes [1]. Ray and mode are two representations of the same propagation behavior in tunnels, and thus theoretically, they should be equivalent. Ahluwalia and Keller [10] mathematically proved ray-mode

Color versions of one or more of the figures in this paper are available online at http://ieeexplore.ieee.org.

Disclaimer

The findings and conclusions in this paper are those of the author(s) and do not necessarily represent the views of the National Institute for Occupational Safety and Health. Mention of any company or product does not constitute endorsement by the NIOSH.

equivalence in acoustics by showing that mode and ray representations of the sound field in a stratified ocean can be transformed from one to the other. The ray-mode equivalence in acoustics has also been discussed by Kamel and Felsen [11], where a cluster of acoustic modes was shown to be equivalent, both in phase and amplitude, to a ray field plus a remainder. Felsen *et al.* [12], [13] extended the ray-mode analysis to the radio world, and proposed a hybrid ray-mode formulation for modeling Green's functions in a 2-D perfectly conducting parallel-plate waveguide. Recently, we mathematically proved the ray-mode equivalence in a 3-D dielectric waveguide (i.e., a general tunnel) in [14]. In addition to the mathematical proof, measurement results at a variety of frequencies are provided in [14] to validate the ray tracing and modal methods.

So far the ray-mode equivalence discussion has been limited to tunnels with smooth walls. It is known that underground mine tunnels often have rough walls, which influence the radio signal propagation in the tunnel. In this paper, we will investigate how surface roughness affects radio propagation in tunnels and discuss the ray-mode equivalence in the presence of wall roughness.

Despite the long history of tunnel propagation research, very few investigations have analyzed the influence of roughness on tunnel propagation. Mahmoud and Wait [15] analyzed the effect of roughness on the radio attenuation in a parallel-plate waveguide in the 1970s. Around the same time, Emslie *et al.* [1] developed probably the earliest model for analyzing the roughness effect in a rectangular tunnel. In [1], an additional mode attenuation constant that accounts for the energy losses caused by the wall roughness to the dominant mode was derived, under the assumption of equal roughness for the four tunnel walls. Emslie's roughness model has been recently used by Fuschini and Falciasecca [2] for road and subway tunnels. It has also been applied in [16] and [17] for modeling the influence of roughness on radio propagation in caves. Some preliminary theoretical studies of applying Emslie's roughness model to coal mines were reported in [8].

The roughness analyses above are based on the modal method, where the roughness effect is modeled by an additional attenuation constant applied to the dominant mode. In addition, there are some other methods used for analyzing the roughness effect. For example, Martelly and Janaswamy [18] numerically calculated the roughness effect using the vector parabolic equation method, and showed it is consistent with Emslie's analytical model given in [1]. A vector finite element-based full wave method is used in [19] to analyze radio propagation in a long cave with rough surfaces. Compared with the modal method, numerical (full wave) methods generally demand significantly more computation resources and provide less physical insight.

In this paper, we proposed a unified ray-mode method for modeling radio propagation in tunnels with rough walls. The contribution of this paper include the following. First, we derived general analytical formulas for modeling the influence of the wall roughness based on the modal and ray tracing methods, respectively. For the modal method, we derived a general roughness attenuation constant for both the dominant mode and higher order modes. In addition to the capability of modeling roughness attenuation for higher modes, the model developed in this paper is more general than Emslie's model in the sense that it can model

radio propagation in tunnels that have different roughnesses on different surfaces. Such flexibility is particularly useful for mines and caves where the roughness condition for each wall could be significantly different. Second, we mathematically proved the equivalence of the ray-mode solution in the presence of wall roughness.

It should be noted that a ray method has been discussed by Emslie *et al.* [1] and later by Fuschini and Falciasecca [2]. This ray method is different from the ray tracing method reported in this paper. The main differences between the "rays" presented in [1] and [2] and the "true rays" presented in this paper include:

1. *Dependence on Modes:* "Rays" are determined by mode angle, while "True rays" are determined by ray tracing, typically through a ray tracing algorithm.
2. *Dependence on Separation Distance:* The intensity of "rays" remains unchanged when the distance varies, while the intensity of the "true rays" decays with distance.
3. *Dependence on Antenna Transversal Location:* The "rays" are independent of antenna location, while the "true rays" are affected by antenna location. For example, "true rays" will change if either the location of the transmitter antenna or the receiver antenna changes.

In summary, "rays" in [1] and [2] are essentially a uniform plane wave representation of modes and thus have been considered as modes in this paper.

The rest of this paper is organized as follows. A roughness-modified reflection coefficient is introduced in Section II. Ray tracing and modal methods for modeling radio propagation in tunnels with rough walls are presented in Section III. The equivalence of the ray tracing and modal methods is also discussed in Section III. Some numerical results and analysis are given in Section IV. Finally, the conclusions are given in Section V.

II. Plane Waves Reflected From Smooth and Rough Surfaces

When a radio wave is incident on a tunnel wall, part of the wave transmits into the wall and the other part is reflected back to the tunnel. It is found that power loss associated with reflections on tunnel walls constitutes the major propagation loss in a tunnel environment [9]. In this section, we will briefly review the theory of plane wave reflection from smooth and rough surfaces, respectively, with a focus on its simplification under the grazing incidence condition.

A. Plane Waves Reflected From a Smooth Surface

For a plane wave incident on a smooth surface, it is known that the wave is reflected in the specular direction, given by Snell's law of reflection. The reflected field can be calculated by multiplying the incident field with the corresponding Fresnel reflection coefficient $\rho_{\perp,//}$, given by [9]

$$\rho_{\perp,//}=\frac{cos\theta_{\perp,//}-\Delta_{\perp,//}}{cos\theta_{\perp,//}+\Delta_{\perp,//}}. \quad (1)$$

Here, the subscripts ⊥ and // denote the perpendicular and parallel polarizations, respectively, and $\theta_{\perp,//}$ is the angle of incidence defined by the angle between the direction of the incident wave and the normal to the surface. $\Delta_{\perp,//}$ is a quantity related to surface impedance, and is given by

$$\Delta_{//}=\frac{\sqrt{\bar{\varepsilon}_{//}-\sin^2\theta_{//}}}{\bar{\varepsilon}_{//}}$$
$$\Delta_{\perp}=\sqrt{\bar{\varepsilon}_{\perp}-\sin^2\theta_{\perp}} \quad (2)$$

where $\bar{\varepsilon}_{//,\perp} = \varepsilon_{//,\perp}/\varepsilon_0$ are the complex relative permittivity. For grazing incidences where the angle of incidence approaches 90°, we can approximate the Fresnel reflection coefficients $\rho_{\perp,//}$ as [9]

$$\rho_{\perp,//} \approx -\exp\left(\frac{-2\cos\theta_{\perp,//}}{\Delta_{\perp,//}}\right) \quad (3)$$

$$\Delta_{//} \approx \frac{\sqrt{\bar{\varepsilon}_{//}-1}}{\bar{\varepsilon}_{//}}\Delta_{\perp} \approx \sqrt{\bar{\varepsilon}_{\perp}-1}. \quad (4)$$

B. Plane Waves Reflected From a Rough Surface

Radio reflection from a rough surface is usually handled by a stochastic method, since the surface roughness can only be measured statistically. Although other distributions are possible [20], the distribution of a reflecting surface variation is often assumed to be a zero mean Gaussian with a standard deviation of σ_h. For a rough reflecting surface, it is known that incident energy will be scattered in angles other than the specular angle of reflection. As a result, radio waves reflected from a rough surface generally include two components—a diffuse component and a specular component. The specular component decreases with increasing surface roughness, whereas the diffuse component becomes more significant. For surfaces that have a slight roughness ($\sigma_h \ll \lambda$), the diffuse component can be ignored, and the specular component can be computed by the same method introduced in II-A, with the corresponding Fresnel reflection coefficients modified by the following roughness attenuation factor [21], [22]:

$$\rho_s = \exp\left\{-8\left(\frac{\pi\,\sigma_h \cos\theta_{\perp,//}}{\lambda}\right)^2\right\}. \quad (5)$$

It is apparent from (5) that the attenuation factor ρ_s is independent of the polarization status of the incident waves. In addition, it is found that ρ_s decreases with the surface roughness σ_h, and increases with the wavelength λ.

It should be noted that the surface becomes perfectly reflecting at extreme grazing incidence ($\theta_{\perp,//} \rightarrow \pi/2$) and (5) satisfies the requirement as $\rho_s = 1$ in this case. One limitation of (5) is that the roughness must be smaller than wavelength as the equation was derived based on a small roughness assumption.

III. Modeling the Influence of Wall Roughness on Tunnel Propagation

We consider a straight hollow dielectric waveguide with rectangular cross-sectional dimensions, as shown in Fig. 1. The coordinate system is oriented in the center of the waveguide cross section, with x horizontal, y vertical, and z down the waveguide. Let $2a$ and $2b$ denote the size of the x and y dimensions, respectively. ε_0 is the permittivity of air, and $\varepsilon_{a,b}$ is the complex permittivity of the vertical and horizontal walls surrounding the waveguide, respectively. The permeability of all the media is assumed to be the same and equal to that of the free space μ_0. A transmitter is located at $T(x_0, y_0, 0)$ and a receiver at $R(x, y, z)$. Both the transmitter antenna and the receiver antenna are assumed to be omnidirectional.

The electric field within a rectangular dielectric waveguide can either be represented by a ray summation based on the ray tracing method, or by a mode summation based on the modal method. In the following, we discuss the two methods for modeling the influence of wall roughness on tunnel propagation in detail.

A. Ray Tracing Method

1) Vertical (y-Direction) Polarization—Based on the ray tracing theory, the electric field at an arbitrary point $R(x, y, z)$ within a rectangular waveguide can be obtained by summing the scalar electric fields of the rays from all the images of a point source [$T(x_0, y_0, 0)$] as [3]

$$E_r^y(x,y,z) = E_t \sum_{m=-\infty}^{+\infty} \sum_{n=-\infty}^{+\infty} \frac{e^{-jkr_{m,n}}}{r_{m,n}} \rho_{\perp}^{|m|} \rho_{//}^{|n|} \quad (6)$$

where the superscript "y" denotes a "y" (vertically) polarized source. E_t is the transmitted electric field, which is a constant determined by the transmitted power. $k = 2\pi/\lambda$ is the free space wave vector. The integers m and n are the orders of the image $I_{m,n}$. The magnitude of m and n is the number of reflections that the ray undergoes relative to the vertical and

horizontal walls, respectively. The signs of m and n indicate whether the image is located on the positive or negative side of the x- and y-axis, respectively. Note that as a special case when $m = n = 0$, the image $I_{0,0}$ becomes the point source itself, and the ray path connecting the image $I_{0,0}$ and the receiver becomes the line-of-sight path. Some examples of the rays and images in a 2-D rectangular tunnel are shown in Fig. 2. The path length $r_{m,n}$ and the coordinate of the image $I_{m,n}$ are given by

$$\begin{aligned} r_{m,n} &= \sqrt{(x_m - x)^2 + (y_n - y)^2 + z^2}5 \\ x_m &= 2ma + (-1)^m x_0 \\ y_n &= 2nb + (-1)^n y_0. \end{aligned} \tag{7}$$

In (6), the reflection coefficient $\rho_{//,\perp}$ for a tunnel with smooth walls is defined in (1) and approximated by (3) under the grazing incidence assumption. The corresponding incident angles and the surface impedances are given by

$$\begin{aligned} \theta_\perp &= \operatorname{acos}\left(\frac{|x_m - x|}{r_{m,n}}\right) \\ \theta_{//} &= \operatorname{acos}\left(\frac{|y_n - y|}{r_{m,n}}\right) \end{aligned} \tag{8}$$

$$\begin{aligned} \Delta_{//} &\approx \frac{\sqrt{\bar{\varepsilon}_b - 1}}{\bar{\varepsilon}_b} \\ \Delta_\perp &\approx \sqrt{\bar{\varepsilon}_a - 1} \end{aligned} \tag{9}$$

where $\bar{\varepsilon}_{a,b} = \varepsilon_{a,b}/\varepsilon_0$ are the complex relative permitivities for the horizontal and vertical walls, normalized by the vacuum permitivity ε_0. $\bar{\varepsilon}_{a,b}$ can be expressed as

$$\bar{\varepsilon}_{a,b} = \bar{\varepsilon}^r_{a,b} - j\frac{\sigma_{a,b}}{2\pi f \varepsilon_0} \tag{10}$$

where $\bar{\varepsilon}^r_{a,b}$ denotes the real part of the relative permitivity $\bar{\varepsilon}_{a,b}$. $\sigma_{a,b}$ are the conductivity of the horizontal and vertical walls, respectively. f is the frequency.

Now, we look at the two reflection coefficients (i.e., $\rho_\perp$ and $\rho_{//}$) in (6) when wall roughnesses are present. Including stochastic rough surface scattering into deterministic ray-optical wave propagation modeling has been discussed in [23], and will be used to characterize the surface roughness in this paper. As shown in Section II-B, the key to modeling radio reflection from a rough surface is introducing a scattering loss factor ρ_s to compensate for the reduced energy in the specular direction for each diffuse reflection. We

assume that the distribution of the surface variation is a zero mean Gaussian with a standard deviation of $\sigma_{h,i}$, where the subscript i denotes the ith wall of the tunnel, with the floor as $i = 1$, as shown in Fig. 3. As a result, the scattering loss factor for the ith wall $\rho_{s,i}^{\perp,//}$ can be expressed as

$$\rho_{s,i}^{\perp,//}=\exp\left\{-8\left(\frac{\pi\,\sigma_{h,i}\cos\theta_{\perp,//}}{\lambda}\right)^2\right\}. \quad (11)$$

Therefore, the electric field inside a tunnel with rough walls can be calculated by

$$E_r^y=E_r\sum_{m=-\infty}^{+\infty}\sum_{n=-\infty}^{+\infty}\frac{e^{-jkr_{m,n}}}{r_{m,n}}\cdot\left(\rho_\perp\sqrt{\rho_{s,2}^{\perp}\rho_{s,4}^{\perp}}\right)^{|m|}\cdot\left(\rho_{//}\sqrt{\rho_{s,1}^{//}\rho_{s,3}^{//}}\right)^{|n|}. \quad (12)$$

2) Horizontal (x-Direction) Polarization—Similarly, for a horizontally polarized source, the electrical field can be calculated as

$$E_r^x=E_t\sum_{m=-\infty}^{+\infty}\sum_{n=-\infty}^{+\infty}\frac{e^{-jkr_{m,n}}}{r_{m,n}}\cdot\left(\rho_\perp\sqrt{\rho_{s,1}^{\perp}\rho_{s,3}^{\perp}}\right)^{|m|}\cdot\left(\rho_{//}\sqrt{\rho_{s,2}^{//}\rho_{s,4}^{//}}\right)^{|n|} \quad (13)$$

where

$$\theta_{//}=\operatorname{acos}\left(\frac{|x_m-x|}{r_{m,n}}\right)$$
$$\theta_\perp=\operatorname{acos}\left(\frac{|y_n-y|}{r_{m,n}}\right) \quad (14)$$

$$\Delta_{//}\approx\frac{\sqrt{\bar{\varepsilon}_a-1}}{\bar{\varepsilon}_a}$$
$$\Delta_\perp\approx\sqrt{\bar{\varepsilon}_b-1}. \quad (15)$$

A comparison between the two electrical field expressions [in (12) and (13)] for the horizontal and vertical polarizations shows that the images and rays are determined by the location of the source and the receiver, and are independent of the polarization of the source. The polarization state influences the received electrical field through the reflection coefficients. When the source polarization switches from one to the other, the corresponding electrical field can be readily computed by switching the associated reflection coefficients.

B. Modal Method

1) Horizontal (x-Direction) Polarization—The modal method views the electrical field in a tunnel as a set of hybrid modes denoted by $EH_{p,q}$, where the subscripts p and q represent the order of the mode. For a horizontally polarized source, the main component of the E-field at an arbitrary observation point $R(x, y, z)$ within a rectangular tunnel can be expressed as [24]

$$E_r^x = E_t \left\{ \sin(k_x x+\varphi_x)+\sin\left[\frac{j\bar{\varepsilon}_a k_x x}{ka\sqrt{\bar{\varepsilon}_a-1}}\right]\cos(k_x x+\varphi_x)\right\}\times\left\{\cos(k_y y+\varphi_y)-\sin\left[\frac{jk_y y}{kb\sqrt{\bar{\varepsilon}_b-1}}\right]\sin(k_y y+\varphi_y)\right\} \quad (16)$$

where $k_x = (m\pi/2a)$, $k_y = (n\pi/2b)$, and $\tilde{k}_z = \beta_{p,q} - j\alpha_{p,q}$ are the wave vector components along the x-, y-, and z-axis, respectively. E_t is the transmitted electrical field which is a constant determined by the transmitted power. Here, $\beta_{p,q}$ is the phase constant, and $\alpha_{p,q}$ is the attenuation constant that characterizes the signal attenuation along the tunnel axial distance (z-axis). The tilde notation $\tilde{X}$ denotes the argument is complex. The two axillary angles $\varphi_{x,y}$ are defined by

$$\varphi_x = \begin{cases} 0 & p \text{ is even} \\ \pi/2 & p \text{ is odd} \end{cases} \quad (17)$$

$$\varphi_y = \begin{cases} 0 & q \text{ is odd} \\ \pi/2 & q \text{ is even.} \end{cases} \quad (18)$$

For electrically large tunnels where $ka \gg 1$ and $kb \gg 1$ are satisfied, (16) can be reduced to

$$E_r^x \approx E_t \sin(k_x x+\varphi_x)\cos(k_y y+\varphi_y)e^{-jk_z z}. \quad (19)$$

It is apparent that (19) reduces to [1, eq. (1)] for the dominant $EH_{1,1}$ mode.

As shown in [9], the hybrid mode $EH_{p,q}$ can be viewed as an average of four plane waves (rays), which are characterized by the following angles: (θ_x, θ_y), $(\theta_x, -\theta_y)$, $(-\theta_x, \theta_y)$, and $(-\theta_x, -\theta_y)$. Here, $\theta_{x,y}$ denote the angle between the ray and the yz and xz plane, respectively. The value of $\theta_{x,y}$ can be calculated as:

$$\theta_y \approx \frac{q\lambda}{4b} \quad (20)$$

$$\theta_x \approx \frac{p\lambda}{4a}. \quad (21)$$

The axial distance $d_{z,x}$ (as shown in Fig. 3) that the ray travels between two successive reflections on the two side walls can be calculated as

$$d_{z,x} \approx \frac{8a^2}{p\lambda}. \quad (22)$$

For tunnels with four smooth walls, the attenuation of the *E*-field caused by all the reflections can be expressed as

$$E_L^x = \left|\frac{E_r^x}{E_t}\right| = |\rho_{//}^{N_y} \cdot \rho_{\perp}^{N_x}| \quad (23)$$

where $|\cdot|$ denotes the magnitude of the argument. $N_{x,y}$ are the number of reflections on the two side walls and on the roof/floor, respectively

$$N_x \approx \frac{p\lambda z}{8a^2}$$
$$N_y \approx \frac{q\lambda z}{8b^2}. \quad (24)$$

Now, we evaluate the radio attenuation in tunnels with rough walls. Again, we introduce the scattering factor $\rho_{s,i}$ to compensate for the roughness effect. Under the assumption of rough walls, the attenuation of the electrical field given in (23) becomes

$$E_L^x = |[\rho_{//}^{N_x}(\rho_{s,2}^{//}\rho_{s,4}^{//})^{N_x/2}] \cdot [\rho_{\perp}^{N_y}(\rho_{s,1}^{\perp}\rho_{s,3}^{\perp})^{N_y/2}]| \quad (25)$$

where

$$\rho_{\perp} \approx -\exp\left(\frac{-2\sin\theta_y}{\sqrt{\bar{\varepsilon}_b - 1}}\right)$$
$$\rho_{//} \approx -\exp\left(\frac{-2\sin\theta_x \bar{\varepsilon}_a}{\sqrt{\bar{\varepsilon}_a - 1}}\right)$$
$$\rho_{s,i}^{\perp,//} = \exp\left\{-8\left(\frac{\pi\,\sigma_{h,i}\sin\theta_{y,x}}{\lambda}\right)^2\right\}. \quad (26)$$

Substituting (24) and (26) into (25) and after some mathematical manipulations shown in Appendix A, we have

$$E_L^x \approx \exp\left\{-(\alpha_{p,q} + \alpha_{p,q}^s)z\right\} \quad (27)$$

where

$$\alpha_{p,q}^x = \frac{1}{b}\left(\frac{q\lambda}{4b}\right)^2 \mathrm{Re}\left\{\frac{1}{\sqrt{\bar{\varepsilon}_b - 1}}\right\} + \frac{1}{a}\left(\frac{p\lambda}{4a}\right)^2 \mathrm{Re}\left\{\frac{\bar{\varepsilon}_a}{\sqrt{\bar{\varepsilon}_a - 1}}\right\} \quad (28)$$

is the attenuation constant for a tunnel with smooth walls, and

$$\alpha_{p,q}^s = \frac{\pi^2\lambda}{32}\left[\frac{p^3}{a^4}\left(\sigma_{h,2}{}^2 + \sigma_{h,4}{}^2\right) + \frac{q^3}{b^4}\left(\sigma_{h,1}{}^2 + \sigma_{h,3}{}^2\right)\right] \quad (29)$$

is the roughness attenuation constant for the $\mathrm{EH}_{p,q}$ mode.

Note that the modal attenuation constant $\alpha_{p,q}$ derived in (28) is consistent with the classic attenuation constant given in [24]. Compared with [24], the derivation of $\alpha_{p,q}$ given in this paper provides more physical insight as it connects the modal attenuation constant directly to the well-known Fresnel refection coefficients.

Equation (29) provides a general model for quickly estimating the power loss caused by wall roughness. For tunnels with equal roughness on the two horizontal surfaces and the two vertical surfaces (i.e., $\sigma_{h,2} = \sigma_{h,4}$ and $\sigma_{h,1} = \sigma_{h,3}$), after some mathematical manipulation, it can be shown that (29) is consistent with the result presented in [2].

For the dominant mode $\mathrm{EH}_{1,1}$, and with the assumption of equal roughness for all the four walls ($\sigma_{h,i} = \sigma_h$), (29) reduces to

$$\alpha_{p,q}^{s}=\frac{\pi^2\lambda\sigma_h^2}{16}\left[\frac{1}{a^4}+\frac{1}{b^4}\right] \quad (30)$$

which is consistent with the roughness loss factor derived in [1]. For tunnels with smooth walls, we have $\sigma_{h,i} = 0$. In this case, the roughness attenuation constant for the $EH_{p,q}$ mode given in (29) becomes zero as expected.

It is shown in (29) that the value of $\alpha_{p,q}^{s}$ increases rapidly (approximately cubically) with the order of the modes. In addition, given the same roughness condition $\sigma_{h,i}$, the power loss caused by the roughness drops rapidly (approximately by the fourth power) with the transversal dimensions of the tunnel. In addition, if the cross section of the tunnel is not square (i.e., $a \neq b$), the roughness on the walls of the greater dimension has an even greater impact on the power attenuation. For example, in a low coal mine scenario, in which the width of the tunnel is much greater than its height, the roughness loss is mainly determined by the roughness condition of the top and the bottom, while the roughness condition on the two ribs (side walls) has less influence. Note that switching the roughness conditions of the two walls in the same dimension, e.g., $\sigma_{h,1}$ and $\sigma_{h,3}$, does not change the overall power attenuation. In other words, for a tunnel with only one rough surface, the propagation behavior is the same no matter whether the rough surface is on the top (ceiling) or the bottom (floor).

A comparison between (5) and (29) shows that the power loss caused by surface roughness increases with wavelength in a tunnel environment (as shown in Fig. 2), but decreases with wavelength in an open space environment with a single reflection surface (as shown in Fig. 4). This difference of the dependence on the wavelength for these two environments appears to be surprising from a ray point of view, considering that the power loss dependence for each individual ray at each reflection is exactly the same for the two environments. The key is that a coherent summation of the electrical field for rays in a tunnel environment dramatically changes the dependence on the wavelength, due to the waveguide effect, which happens to impose a stronger frequency dependence. The difference of dependence on the wavelength probably is more straightforward if we examine it from the mode point of view. For example, for the $EH_{p,q}$ mode, both the incident angle [given in (20) and (21)] and the number of reflections [shown in (24)] increase with the wavelength, which causes a significant increase of power loss (mainly the loss caused by reflections) with wavelength. While the loss caused by roughness decreases with wavelength, the first two factors, the angle of incidence and number of reflections, turn out to be the two more dominant factors. Therefore, the net effect from all the three factors leads to an overall loss that increases with wavelength.

2) Vertical (y-Direction) Polarization—By following a similar procedure given in Section III-B.1, the modal attenuation constant for the vertical polarization case can be derived as:

$$\alpha_{p,q}^{y}=\frac{1}{a}\left(\frac{p\lambda}{4a}\right)^{2}\mathrm{Re}\left\{\frac{1}{\sqrt{\bar{\varepsilon}_a-1}}\right\}+\frac{1}{b}\left(\frac{q\lambda}{4b}\right)^{2}\mathrm{Re}\left\{\frac{\bar{\varepsilon}_b}{\sqrt{\bar{\varepsilon}_b-1}}\right\}. \quad (31)$$

The roughness modal attenuation constant $\alpha_{p,q}^{s}$ for the vertical polarization case is exactly the same as the horizontal polarization case and is given by (29).

A comparison between (28) and (31) shows that the modal attenuation constant for one polarization can be readily obtained from the other by switching the variables in Table I from one row to the other.

C. Equivalence of the Ray Tracing and Modal Methods

For the ray tracing method, the roughness effect is taken into account by applying a modified Fresnel reflection coefficient to each ray as the ray is reflected by different tunnel walls. For the modal method, the modified Fresnel reflection coefficient is applied to each mode, which is viewed as a mixture of four plane waves. The two methods are two different views of the same problem, and thus should be mathematically equivalent. Equation (32), as shown at the bottom of this page, proves such a ray-mode equivalence with wall roughness taken into consideration, by showing that the ray summation based on the ray tracing method can be converged to the mode summation based on the modal method. In (32), the eigenmode function $A_{p,q}$ and the phase constant $\beta_{p,q}$ are defined by

$$A_{p,q}=\sin\left(\frac{p\pi}{2a}x+\overline{\varphi}_p\right)\sin\left(\frac{q\pi}{2b}y+\overline{\varphi}_q\right)\times\sin\left(\frac{p\pi}{2a}x_0+\overline{\varphi}_p\right)\sin\left(\frac{q\pi}{2b}y_0+\overline{\varphi}_q\right)$$
$$\beta_{p,q}=\sqrt{k^2-\left(\frac{p\pi}{2a}\right)^2-\left(\frac{q\pi}{2b}\right)^2} \quad (33)$$

where

$$\overline{\varphi}_{p,q}=\begin{cases}0 & \text{p, q is even}\\ \pi/2 & \text{p, q is odd}\end{cases} \quad (34)$$

$$E_t\sum_{m=-\infty}^{+\infty}\sum_{n=-\infty}^{+\infty}\frac{e^{-jkr_{m,n}}}{r_{m,n}}\cdot\left(\rho_{\perp}\sqrt{\rho_{s,2}^{\perp}\rho_{s,4}^{\perp}}\right)^{|m|}\cdot\left(\rho_{//}\sqrt{\rho_{s,1}^{//}\rho_{s,3}^{//}}\right)^{|n|}\approx\frac{-j2\pi E_t}{ab}\cdot\sum_{p=1}^{+\infty}\sum_{q=1}^{+\infty}A_{p,q}\frac{e^{-(\alpha_{p,q}+\alpha_{p,q}^{s}+j\beta_{p,q})z}}{\beta_{p,q}} \quad (32)$$

The detailed mathematical proof of (32) is given in Appendix B.

It should be noted that the influence of both transmit and receive antennas' positions on tunnel propagation has been modeled in $A_{p,q}$ by a series of sinusoidal functions [25]. It is apparent from $A_{p,q}$ that the electrical field (and thus power) for the dominant $EH_{1,1}$ is minimized when either the transmitter or the receiver is close to any of the four tunnel walls, and is maximized when antennas are located in the center ($x = 0$, $y = 0$, $x_0 = 0$, $y_0 = 0$). This finding has been recently confirmed by measurement results in a train tunnel in [25].

A close examination of (32) reveals that this roughness model has incorporated all the major controlling factors: tunnel dimensions, frequency, polarization, wall electrical properties, and surface roughness. As a result, (32) provides a unified ray-mode solution to a general tunnel propagation problem.

In Appendix B, we show that the modal roughness attenuation constant $\alpha_{p,q}^{s}$ can be derived based on the ray summation given in (13). The derivation in Appendix B is based on the vertical polarization assumption, but the ray-mode equivalence for the horizontal polarization case can be proved following a similar procedure given in Appendix B. It is interesting to note that in (12), the index of the images (i.e., m and n) starts from minus infinity, while the index of modes (p and q) starts from 1. Both p and q are greater than zero, because only hybrid modes $EH_{p,q}$ are supported in a tunnel environment. In addition, large k and large z are two important assumptions made in the derivation in Appendix A. In other words, ray-mode equivalence only holds for high frequency signals and in the far zone, where the receiver is separated far from the transmitter.

IV. Results and Discussion

Ideally, the proposed model should be validated with measurement results in a tunnel with rough surfaces. However, adding controlled surface roughness to a physical tunnel is not very feasible in practical, as we are trying to introduce a stochastic method (based on roughness definition) into a deterministic problem. As a compromise, we will add simulated roughness to a physical tunnel with smooth surfaces and compare numerical results generated based on different modeling methods.

Recently, extensive RF measurements have been performed in a concrete tunnel to support ultrahigh frequency propagation model development research at the National Institute for Occupational Safety and Health [9]. To investigate how surface roughness affects radio propagation in tunnels, we apply the roughness model given in (32) to compute received signal power within the concrete tunnel. Considering that the actual tunnel where the measurements were performed has very smooth walls, we intentionally add surface roughness onto the tunnel walls in our simulations and investigate how simulated received power varies with surface roughness at different frequencies. Fig. 5 shows a comparison between the simulated power distribution along the center line of a tunnel at three frequencies (i.e., 455, 915, and 2450 MHz) for the vertical polarization. It is assumed that the surface roughnesses for all four tunnel walls are the same and equal to σ_h. As two examples, $\sigma_h = 0$ (i.e., smooth surface) and $\sigma_h = 10$ cm have been simulated and the results are shown in Fig. 5 for comparison. The measured power distributions in the concrete tunnel with smooth walls have also been plotted for reference. The details of the measurement can

be found in [3]. The major parameters used in the simulations are summarized in Table II. The parameters in Table II were chosen fully based on physical parameters used in the measurements except the electrical properties (the relative permittivity and conductivity) of tunnel walls, which were selected based on best fit between the simulation results and the measurement results.

It can be found from Fig. 5 that the simulated results based on the modal (dashed green lines) and ray tracing (red dashed-dotted lines) agree with each other well, for both with and without surface roughnesses scenarios. In addition, the simulation results corresponding to $\sigma_h = 0$ match the measurement results for all tested frequencies as expected. It is apparent that wall roughness introduces additional attenuation to RF signals as well as "smoothness" to the power distribution curve. The "smoothness" effect is due to the fact that higher order modes are attenuated more by the wall roughness than the dominant mode, and therefore, the rapid fading caused by the presence of higher order modes is quickly eliminated. In Fig. 5, the measured signal power for the 455-MHz signal quickly drops with distance for the first 170 m, but remains about the same for distances greater than 170 m. This is due to the limitation of the power measurement equipment, which has a noise floor at about −120 dBm. In other words, the equipment used in the measurement cannot measure power change when the power drops below −120 dBm.

Fig. 6 shows the corresponding power decay profiles for the horizontal polarization scenario. Noticeable discrepancies between the ray tracing and modal simulation results are observed at 455 MHz in Fig. 6. These discrepancies are due to the fact that the ray tracing and modal methods are only equivalent at high frequencies. The additional attenuation caused by wall roughness and its "smoothness" effect are also apparent in Fig. 6.

Fig. 7 shows the power decay profile for the same tunnel, but with different roughnesses on different walls, at 915 MHz, and under the vertical polarization. Again, the good agreement between the results generated by the ray tracing and modal results confirms that ray tracing and modal methods are equivalent, and can be applied to model radio propagation in complicated tunnels that have different surface roughnesses on different walls.

To investigate the ray-mode equivalence at short distances, the results for the first 60 m in Fig. 7 are zoomed in and shown in Fig. 8. It is evident from Fig. 8 that the ray and mode curves do not show good agreement when the separation distance is short (e.g., for $d < 15$ m). The two curves gradually merge together as the distance increases. This observation confirms that ray-mode equivalence only holds when the separation distance is sufficiently far as indicated in Appendix B.

V. Conclusion

This paper investigates the influence of wall roughness on radio propagation in tunnels and mines. Analytical solutions based on the ray tracing and modal methods are derived, respectively, and shown to be equivalent when the frequencies of interest are high and the separation distance between the transmitter and the receiver is sufficiently far. It is found that surface roughness in tunnels introduces additional attenuation to RF signals. The

additional attention caused by surface roughness decreases with tunnel dimensions rapidly and linearly increases with wavelength. The developed models are useful for understanding and analyzing radio propagation in mines, where surface roughnesses are generally significant.

Acknowledgments

The author would like to thank R. Jacksha and T. Plass for their help on taking the measurement data. He would also like to thank Dr. J. Waynert, L. Ko, J. Schall, and A. Mayton for reviewing the manuscript.

References

1. Emslie A, Lagace R, Strong P. Theory of the propagation of UHF radio waves in coal mine tunnels. IEEE Trans Antennas Propag. Mar; 1975 23(2):192–205.
2. Fuschini F, Falciasecca G. A mixed rays—Modes approach to the propagation in real road and railway tunnels. IEEE Trans Antennas Propag. Feb; 2012 60(2):1095–1105.
3. Zhou, C., Waynert, J., Plass, T., Jacksha, R. Modeling RF propagation in tunnels. Proc. IEEE Int. Symp. Antennas Propag. (APS); Orlando, FL, USA. Jul. 2013; p. 1916-1917.
4. Sun Z, Akyildiz IF. Channel modeling and analysis for wireless networks in underground mines and road tunnels. IEEE Trans Commun. Jun; 2010 58(6):1758–1768.
5. Zhou, C., Waynert, J. Modeling the influence of wall roughness on tunnel propagation. Proc. IEEE Radio Wireless Symp. (RWS); Jan. 2014; p. 109-111.
6. Boutin M, Benzakour A, Despins CL, Affes S. Radio wave characterization and modeling in underground mine tunnels. IEEE Trans Antennas Propag. Feb; 2008 56(2):540–549.
7. Liénard M, Degauque P. Natural wave propagation in mine environments. IEEE Trans Antennas Propag. Sep; 2000 48(9):1326–1339.
8. Xu, Z., Huo, Y., Zheng, H-D. The effect of the wall roughness on the electromagnetic wave propagation in coal mine underground. Proc. IEEE Int. Symp. Knowl. Acquisition Modeling; Sep. 2008; p. 482-485.
9. Zhou C, Waynert J, Plass T, Jacksha R. Attenuation constants of radio waves in lossy-walled rectangular waveguides. Prog Electromagn Res. 2013; 142:75–105.
10. Ahluwalia, DS., Keller, JB. Wave Propagation and Underwater Acoustics. Berlin, Germany: Springer; 1977. Exact and asymptotic representations of the sound field in a stratified ocean; p. 14-85.
11. Kamel A, Felsen LB. On the ray equivalent of a group of modes. J Acoust Soc Amer. 1982; 71(6): 1445–1452.
12. Felsen LB, Akleman F, Sevgi L. Wave propagation inside a two-dimensional perfectly conducting parallel-plate waveguide: Hybrid ray-mode techniques and their visualizations. IEEE Antennas Propag Mag. Dec; 2004 46(6):69–89.
13. Felsen LB, Kamel AH. Hybrid ray-mode formulation of parallel plane waveguide Green's functions. IEEE Trans Antennas Propag. Jul; 1981 29(4):637–649.
14. Zhou C, Waynert J. The equivalence of the ray tracing and modal methods for modeling radio propagation in lossy rectangular tunnels. IEEE Antennas Wireless Propag Lett. Mar.2014 13:615–618.
15. Mahmoud S, Wait J. Geometrical optical approach for electromagnetic wave propagation in rectangular mine tunnels. Radio Sci. 1974; 9(12):1147–1158.
16. Rak M, Pechac P. UHF propagation in caves and subterranean galleries. IEEE Trans Antennas Propag. Apr; 2007 55(4):1134–1138.
17. Remley, KA., Koepke, G., Camell, DG., Grosvenor, C., Hough, G., Johnk, RT. Wireless communications in tunnels for urban search and rescue robots. Proc. 8th Workshop Perform. Metrics Intell. Syst; Aug. 2008; p. 236-243.
18. Martelly R, Janaswamy R. An ADI-PE approach for modeling radio transmission loss in tunnels. IEEE Trans Antennas Propag. Jun; 2009 57(6):1759–1770.

19. Pingenot J, Rieben RN, White DA, Dudley DG. Full wave analysis of RF signal attenuation in a lossy rough surface cave using a high order time domain vector finite element method. J Electromagn Waves Appl. 2006; 20(12):1695–1705.
20. Cocheril Y, Vauzelle R. A new ray-tracing based wave propagation model including rough surfaces scattering. Prog Electromagn Res. 2007; 75:357–381. [Online]. Available: http://www.jpier.org/pier/pier.php?paper=07061202. DOI: 10.2528/PIER07061202
21. Ament W. Toward a theory of reflection by a rough surface. Proc IRE. 1953; 41(1):142–146.
22. Davies H. The reflection of electromagnetic waves from a rough surface. Proc IEE Inst Monogr. Aug; 1954 101(7):209–214.
23. Didascalou D, Dottling M, Geng N, Wiesbeck W. An approach to include stochastic rough surface scattering into deterministic ray-optical wave propagation modeling. IEEE Trans Antennas Propag. Jul; 2003 51(7):1508–1515.
24. Laakmann KD, Steier WH. Waveguides: Characteristic modes of hollow rectangular dielectric waveguides. Appl Opt. 1976; 15(5):1334–1340. [PubMed: 20165176]
25. Zhou, C., Jacksha, R. Modeling and measurement the influence of antenna transversal position on tunnel propagation. Proc. IEEE Int. Symp. Antennas Propag. (APS); Vancouver, BC, Canada. Jul. 2015; p. 81-82.

Biography

Chenming Zhou received the Ph.D. degree in electrical engineering from Tennessee Technological University, Cookeville, TN, USA, in 2008. He is a Senior Research Engineer with the National Institute for Occupational Safety and Health (NIOSH), Centers for Disease Control and Prevention (CDC), U.S. Department of Health and Human Services, Pittsburgh, PA, USA. He served as the Project Leader and Principal Investigator for the wireless communications and tracking project, and later the Internet of Things (IoT) for underground coal mines project at NIOSH. He also serves as a government Contract Officer Representative (COR) for NIOSH Broad Agency Announcement (BAA) contracts related to communications and tracking research. Prior to joining NIOSH in August 2012, he was a Research Fellow at the Disney Research Laboratory in Pittsburgh, where he conducted research in RF ranging based on passive RFID tags. Before he started his career in industry at Disney, he was a Project Research Scientist with the Department of Electrical and Computer Engineering, Carnegie Mellon University, Pittsburgh. He holds two U.S. patents in RFID and is the author or co-author of more than 50 technical papers published in peer-reviewed journals or conference proceedings. He is currently an Associate Editor for the *IEEE Antennas and Propagation Magazine*.

Appendix A. Derivation of Modal Attenuation Constant for Tunnels With Rough Walls

Substituting (24) and (26) into (25), we have

$$E_L^x = \left| \exp\left\{ \frac{-2N_y \sin\theta_y}{\sqrt{\bar{\varepsilon}_b - 1}} + \frac{-2N_x \bar{\varepsilon}_a \sin\theta_x}{\sqrt{\bar{\varepsilon}_a - 1}} \right\} \right| \cdot \exp\left\{ -4N_y \left(\frac{\pi \sin\theta_y}{\lambda} \right)^2 \left(\sigma_{h,1}^2 + \sigma_{h,3}^2 \right) \right\} \cdot \exp\left\{ -4N_x \left(\frac{\pi \sin\theta_x}{\lambda} \right)^2 \left(\sigma_{h,2}^2 + \sigma_{h,4}^2 \right) \right\}. \quad (35)$$

Applying the small angle approximation $\sin \theta_{x,y} \approx \theta_{x,y}$ to (35), and then substituting (20), (21), and (24) into (35) leads to

$$E_L^x \approx \left| \exp\left\{ -\frac{\lambda^2 z}{16} \left(\frac{q^2}{b^3 \sqrt{\bar{\varepsilon}_b - 1}} + \frac{p^2 \bar{\varepsilon}_a}{a^3 \sqrt{\bar{\varepsilon}_a - 1}} \right) \right\} \right| \cdot \exp\left\{ -\frac{\pi^2 \lambda z}{32} \left[\frac{q^3}{b^4} \left(\sigma_{h,1}^2 + \sigma_{h,3}^2 \right) + \frac{p^3}{a^4} \left(\sigma_{h,2}^2 + \sigma_{h,4}^2 \right) \right] \right\} = \exp\left\{ -(\alpha_{p,q} + \alpha_{p,q}^s) z \right\} \quad (36)$$

where

$$\alpha_{p,q} = \frac{1}{a} \left(\frac{p\lambda}{4a} \right)^2 \mathrm{Re}\left\{ \frac{\bar{\varepsilon}_a}{\sqrt{\bar{\varepsilon}_a - 1}} \right\} + \frac{1}{b} \left(\frac{q\lambda}{4b} \right)^2 \mathrm{Re}\left\{ \frac{1}{\sqrt{\bar{\varepsilon}_b - 1}} \right\} \quad (37)$$

and

$$\alpha_{p,q}^s = \frac{\pi^2 \lambda}{32} \left[\frac{p^3}{a^4} \left({\sigma_{h,2}}^2 + {\sigma_{h,4}}^2 \right) + \frac{q^3}{b^4} \left({\sigma_{h,1}}^2 + {\sigma_{h,3}}^2 \right) \right]. \quad (38)$$

In (37), Re{·} denotes the real part of the argument.

Appendix B. Proof of Ray-Mode Equivalence for Tunnels With Rough Walls

Substituting [7]–[9] into (3) yields

$$\rho_\perp \approx -\exp\left(\frac{-2|x_m - x|}{\sqrt{\bar{\varepsilon}_a - 1}} \right) \quad (39)$$

$$\rho_{//} \approx -\exp\left(\frac{-2|y_n-y|\varepsilon_b}{\sqrt{\varepsilon_b-1}}\right). \quad (40)$$

Substituting (7), (11) (39), and (40) into (12) leads to

$$E_r^y = E_t \sum_{m=-\infty}^{+\infty}\sum_{n=-\infty}^{+\infty} \frac{e^{-jkr_{m,n}}}{r_{m,n}} \cdot e^{-(U_1+U_2+U_3)} \quad (41)$$

where

$$\begin{aligned} U_1 &= \frac{2}{r_{m,n}}\left(\frac{|x_m-x||m|}{\sqrt{\varepsilon_a-1}}+\frac{|y_n-y||n|\varepsilon_b}{\sqrt{\varepsilon_b-1}}\right) \\ U_2 &= 8\left(\frac{\pi}{\lambda}\cdot\frac{|x_m-x|}{r_{m,n}}\right)^2\left(\frac{\sigma_{h,1}^2+\sigma_{h,3}^2}{2}\right)|m| \\ U_3 &= 8\left(\frac{\pi}{\lambda}\cdot\frac{|y_n-y|}{r_{m,n}}\right)^2\left(\frac{\sigma_{h,2}^2+\sigma_{h,4}^2}{2}\right)|n|. \end{aligned} \quad (42)$$

Following the procedures introduced in [14]:

$$E_r^y = E_t \sum_{s_1=-\infty}^{+\infty}\sum_{s_2=\infty}^{+\infty}\sum_{l=1}^{4}(-1)^{l+1} f_l(t_1,t_2) \quad (43)$$

where

$$f_l(t_1,t_2) = \frac{1}{\sqrt{t_1^2+t_2^2+z^2}} e^{-(jk\sqrt{t_1^2+t_2^2+z^2}+\breve{U}_1+\breve{U}_2+\breve{U}_3)} \quad (44)$$

in (44)

$$\begin{aligned} t_1 &= x_m - x = 2ma + \tilde{x}_l \\ t_2 &= y_m - y = 2nb + \tilde{y}_l \end{aligned} \quad (45)$$

$$\breve{U}_1(t_1,t_2)=\frac{1}{\sqrt{t_1^2+t_2^2+z^2}}\cdot\left[\frac{|t_1(t_1-\tilde{x}_l)|}{a\sqrt{\tilde{\varepsilon}_a-1}}+\frac{|t_2(t_2-\tilde{y}_l)\tilde{\varepsilon}_b|}{b\sqrt{\tilde{\varepsilon}_b-1}}\right]$$
$$\breve{U}_2(t_1,t_2)=-\frac{k^2}{2a}\cdot\frac{|t_1^2(t_1-\tilde{x}_l)|}{t_1^2+t_2^2+z^2}\cdot\left(\sigma_{h,2}^2+\sigma_{h,4}^2\right)$$
$$\breve{U}_3(t_1,t_2)=-\frac{k^2}{2b}\cdot\frac{|t_1^2(t_1-\tilde{y}_l)|}{t_1^2+t_2^2+z^2}\cdot\left(\sigma_{h,1}^2+\sigma_{h,3}^2\right). \quad (46)$$

To separate the even and odd instances of the image order m and n, we introduce two integers s_1 and s_2 to reformulate t_1 and t_2, respectively

$$t_1=4s_1a+\overline{x}_l$$
$$t_2=4s_2b+\overline{y}_l. \quad (47)$$

The values of the aiding variables, such as $\bar{x}_l$ and $\bar{y}_l$, are summarized in Table III.

With the help of the Poisson summation formula, we can convert $f_l(t_1, t_2)$ into its 2-D Fourier transform $\hat{f}_l(p, q)$ [14]

$$\sum_{s_1=-\infty}^{+\infty}\sum_{s_2=-\infty}^{+\infty}f_l(2\pi s_1,2\pi s_2)=\sum_{p=-\infty}^{+\infty}\sum_{q=-\infty}^{+\infty}\hat{f}_l(p,q) \quad (48)$$

where

$$\hat{f}_l(p,q)=\frac{1}{(2\pi)^2}\int_{-\infty}^{\infty}\int_{-\infty}^{\infty}f_l(\tau_1,\tau_2)e^{-j(ps_1+qs_2)}d\tau_1d\tau_2. \quad (49)$$

Substituting (44) into (49) leads to

$$\hat{f}_l(p,q)=\frac{1}{(2\pi)^2}\int_{-\infty}^{\infty}\int_{-\infty}^{\infty}B(\tau_1,\tau_2)e^{-jk\Phi(\tau_1,\tau_2)}d\tau_1d\tau_2 \quad (50)$$

where

$$B(\tau_1,\tau_2)=\frac{1}{\sqrt{\tau_1^2+\tau_2^2+z^2}}e^{-|\breve{U}_1(\tau_1,\tau_2)+\breve{U}_2(\tau_1,\tau_2)+\breve{U}_3(\tau_1,\tau_2)|}$$

and

$$\Phi(\tau_1,\tau_2)=\sqrt{\tau_1^2+\tau_2^2+z^2}+\frac{p\tau_1+q\tau_2}{k}. \quad (51)$$

The integral in (50) can be evaluated based on the principle of stationary phase for large k [14]. The following stationary points can be obtained by solving the equations $(\partial\Phi/\partial\boldsymbol{\tau}_1) = 0$ and $(\partial\Phi/\partial\boldsymbol{\tau}_2) = 0$:

$$\begin{aligned}\tau_{10}&=\frac{-pz}{\sqrt{k^2-p^2-q^2}}\\ \tau_{20}&=\frac{-qz}{\sqrt{k^2-p^2-q^2}}.\end{aligned} \quad (52)$$

As a result, the integral in (50) can be approximated as

$$\hat{f}_l(p,q)\approx\frac{B(\tau_{10},\tau_{20})}{j2\pi k\sqrt{\det[\Psi]}}\exp\{-jk\Phi(\tau_{10},\tau_{20})\} \quad (53)$$

where det [Ψ] denotes the determinant of the matrix Ψ and

$$\Psi_{i,j}=\frac{\partial^2\Phi}{\partial\tau_i\partial\tau_j}\Big|_{\tau_{10},\tau_{20}}. \quad (54)$$

We assume that the separation distance z is sufficiently large, such that the following approximations hold:

$$\begin{aligned}\tau_{10}-\tilde{x}_l&\approx\tau_{10}\\ \tau_{20}-\tilde{y}_l&\approx\tau_{20}.\end{aligned} \quad (55)$$

Substituting the stationary point expression in (52) into (53) and applying approximations in (55) leads to

$$B(\tau_{10},\tau_{20})\approx\frac{\sqrt{k^2-p^2-q^2}}{kz}\cdot e^{-(\breve{U}_1+\breve{U}_2+\breve{U}_3)} \quad (56)$$

where

$$\begin{aligned}\check{U}_1(p,q)&=\left[\frac{p^2}{a\sqrt{\bar{\varepsilon}_a-1}}+\frac{q^2\bar{\varepsilon}_b}{b\sqrt{\bar{\varepsilon}_b-1}}\right]\cdot\frac{z}{k\sqrt{k^2-p^2-q^2}}\\ \check{U}_2(p,q)&=\frac{p^3z}{2a\sqrt{k^2-p^2-q^2}}\cdot(\sigma_{h,2}^2+\sigma_{h,4}^2)\\ \check{U}_3(p,q)&=\frac{q^3z}{2b\sqrt{k^2-p^2-q^2}}\cdot(\sigma_{h,1}^2+\sigma_{h,3}^2).\end{aligned}\tag{57}$$

For electrically large tunnels where $k \gg p$ and $k \gg q$, we have

$$\begin{aligned}\check{U}_1(p,q)&\approx\left[\frac{p^2}{a\sqrt{\bar{\varepsilon}_a-1}}+\frac{q^2\bar{\varepsilon}_b}{b\sqrt{\bar{\varepsilon}_b-1}}\right]\cdot\frac{z}{k^2}\\ \check{U}_2(p,q)&\approx\frac{p^3z}{2ak}\cdot(\sigma_{h,2}^2+\sigma_{h,4}^2)\\ \check{U}_3(p,q)&\approx\frac{q^3z}{2bk}\cdot(\sigma_{h,1}^2+\sigma_{h,3}^2).\end{aligned}\tag{58}$$

Substituting (52) into (51) and then (54) yields

$$\begin{aligned}\Phi(\tau_{10},\tau_{20})&=\frac{z}{k}\sqrt{k^2-p^2-q^2}\\ \det[\Psi]&=\frac{(k^2-p^2-q^2)^2}{k^4z^2}.\end{aligned}\tag{59}$$

Substituting (56) and (59) into (53), we have

$$\hat{f}_l(p,q)\approx\frac{e^{-(jz\sqrt{k^2-p^2-q^2}+\check{U}_1+\check{U}_1+\check{U}_3)}}{j2\pi\sqrt{k^2-p^2-q^2}}.\tag{60}$$

Based on (47), the integer $s_{1,2}$ can be represented by $t_{1,2}$ as

$$\begin{aligned}2\pi s_1&=\frac{(t_1-\overline{x}_l)\pi}{2a}\\ 2\pi s_2&=\frac{(t_2-\overline{y}_l)\pi}{2b}.\end{aligned}\tag{61}$$

Substituting (61) into (48) and applying the shift and scaling properties of the Fourier transform, we have

$$f_l(t_1,t_2)=\frac{\pi^2}{4ab}\hat{f}_l\left(\frac{p\pi}{2a},\frac{q\pi}{2b}\right)e^{j\left(\frac{p\pi}{2a}\overline{x}_l+\frac{q\pi}{2b}\overline{y}_l\right)}. \quad (62)$$

Substituting (62) into (43) yields

$$E_r^y=\frac{E_t\pi^2}{4ab}\sum_{p=-\infty}^{+\infty}\sum_{q=-\infty}^{+\infty}\hat{f}\left(\frac{p\pi}{2a},\frac{q\pi}{2b}\right)\sum_{l=1}^{4}(-1)^{l+1}\times e^{j\left(\frac{p\pi}{2a}\overline{x}_l+\frac{q\pi}{2b}\overline{y}_l\right)}. \quad (63)$$

Note that in (63), the subscript "*l*" has been dropped from the function $\hat{f}_l((p\pi/2a),(q\pi 2b))$, and thus, the function $\hat{f}_l$ can be factored out. Based on (58) and (60), the function $\hat{f}((p\pi/2a),(q\pi/2b))$ can be expressed as

$$\hat{f}\left(\frac{p\pi}{2a},\frac{q\pi}{2b}\right)\approx\frac{e^{-(\alpha_{p,q}+\alpha_{p,q}^s+j\beta_{p,q})z}}{j2\pi\sqrt{k^2-\left(\frac{p\pi}{2a}\right)^2-\left(\frac{q\pi}{2b}\right)^2}} \quad (64)$$

where $\alpha_{p,q}$ is the modal attenuation constant defined by (31) and $\alpha_{p,q}^s$ is the roughness modal attenuation constant defined by (29). $\beta_{p,q}$ is the axial propagation constant defined as

$$\beta_{p,q}=\sqrt{k^2-\left(\frac{p\pi}{2a}\right)^2-\left(\frac{q\pi}{2b}\right)^2}. \quad (65)$$

It has been shown in the appendix of [14] that

$$\sum_{l=1}^{4}(-1)^{l+1}e^{j\left(\frac{p\pi}{2a}\overline{x}_l+\frac{q\pi}{2b}\overline{y}_l\right)}=16\sin\left(\frac{p\pi}{2a}x+\overline{\varphi}_p\right)\sin\left(\frac{q\pi}{2b}y+\overline{\varphi}_q\right)\times\sin\left(\frac{p\pi}{2a}x_0+\overline{\varphi}_p\right)\sin\left(\frac{q\pi}{2b}y_0+\overline{\varphi}_q\right) \quad (66)$$

where

$$\overline{\varphi}_{p,q}=\begin{cases}0 & p,q\ \text{is even}\\ \pi/2 & p,q\ \text{is odd.}\end{cases} \quad (67)$$

Substituting (64) and (66) into (63) yields

$$E_r^y = \frac{-j2\pi\, E_t}{ab} \sum_{p=1}^{+\infty} \sum_{q=1}^{+\infty} A_{p,q} \frac{e^{-(\alpha_{p,q}^y + \alpha_{p,q}^s + j\beta_{p,q})z}}{\beta_{p,q}} \quad (68)$$

where

$$A_{p,q} = \sin\left(\frac{p\pi}{2a}x + \overline{\varphi}_p\right) \sin\left(\frac{q\pi}{2b}y + \overline{\varphi}_q\right) \times \sin\left(\frac{p\pi}{2a}x_0 + \overline{\varphi}_p\right) \sin\left(\frac{q\pi}{2b}y_0 + \overline{\varphi}_q\right). \quad (69)$$

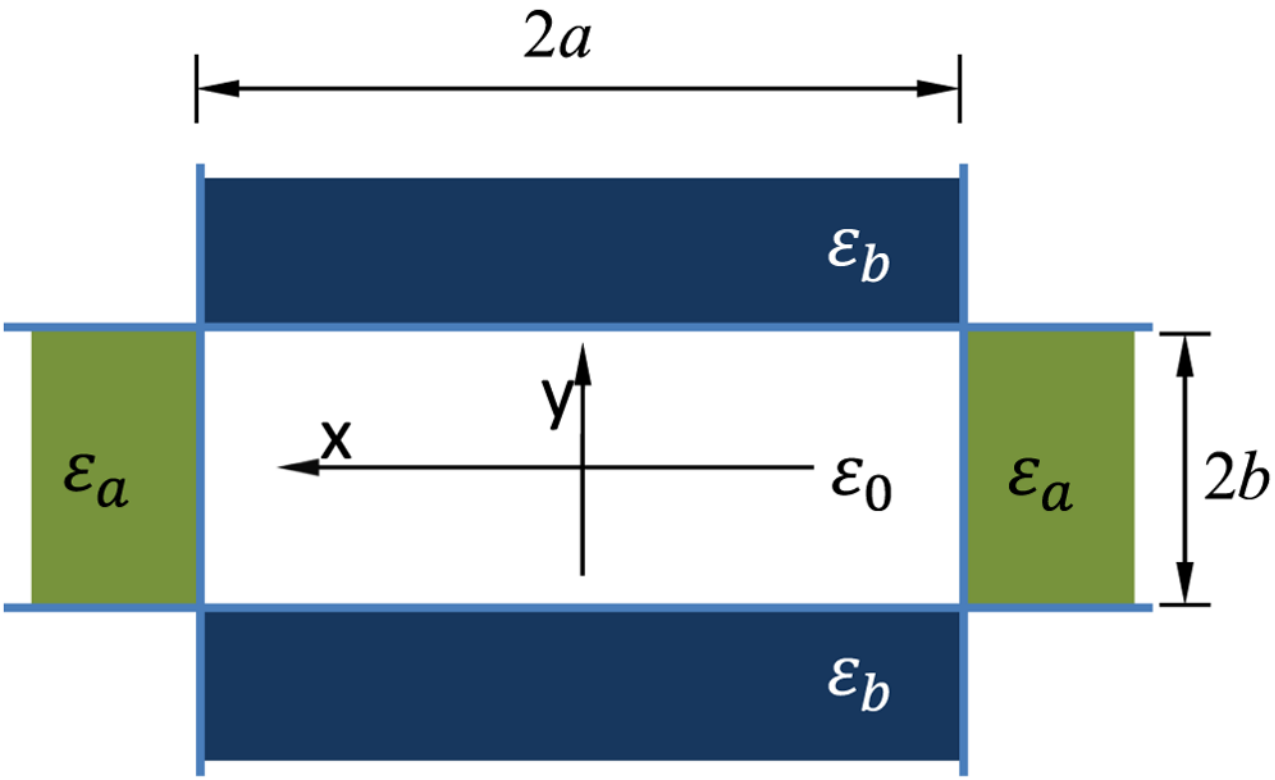

Fig. 1.
Cross section of a hollow dielectric waveguide.

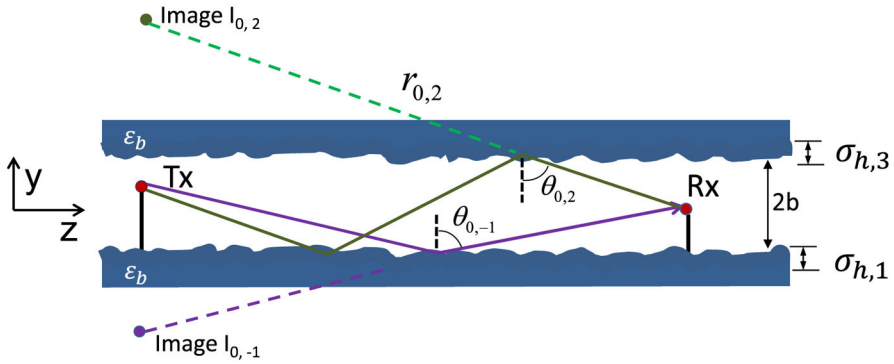

Fig. 2.

Ray tracing method for modeling the influence of wall roughness on radio propagation in tunnels.

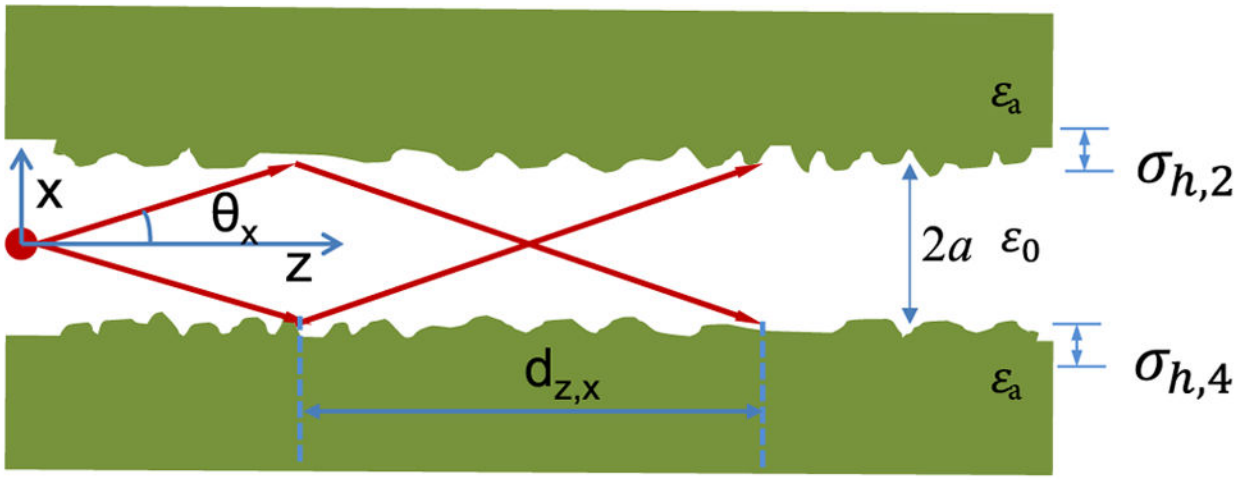

Fig. 3.
Modal method for modeling the influence of wall roughness on radio propagation in tunnels.

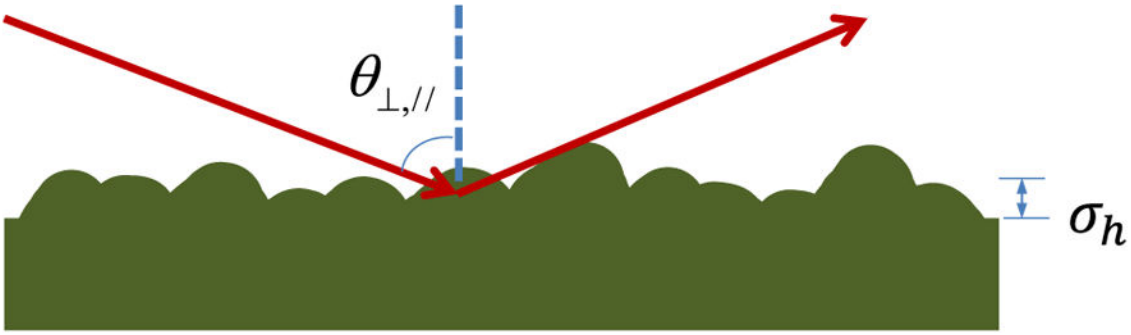

Fig. 4.
Radio reflection from a rough surface.

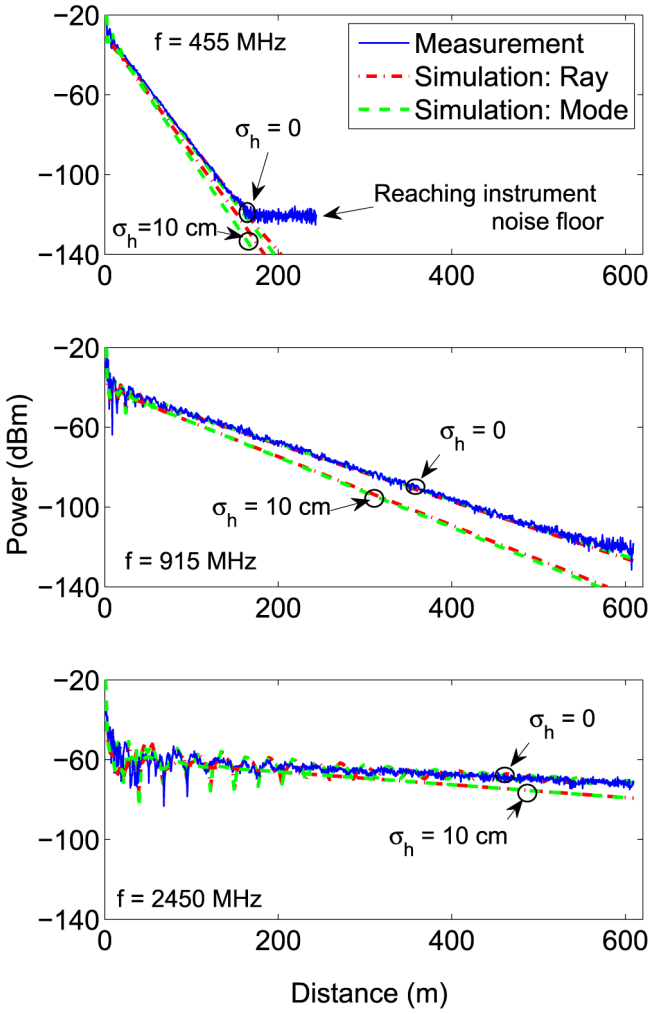

Fig. 5.
Influence of surface roughness on tunnel propagation: vertical polarization.

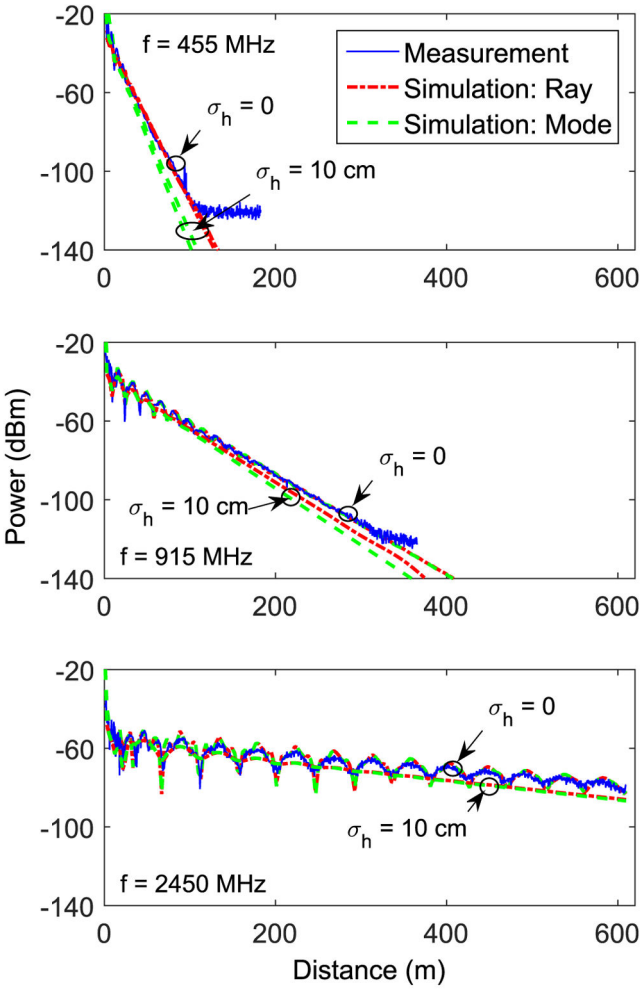

Fig. 6.
Influence of surface roughness on tunnel propagation: horizontal polarization.

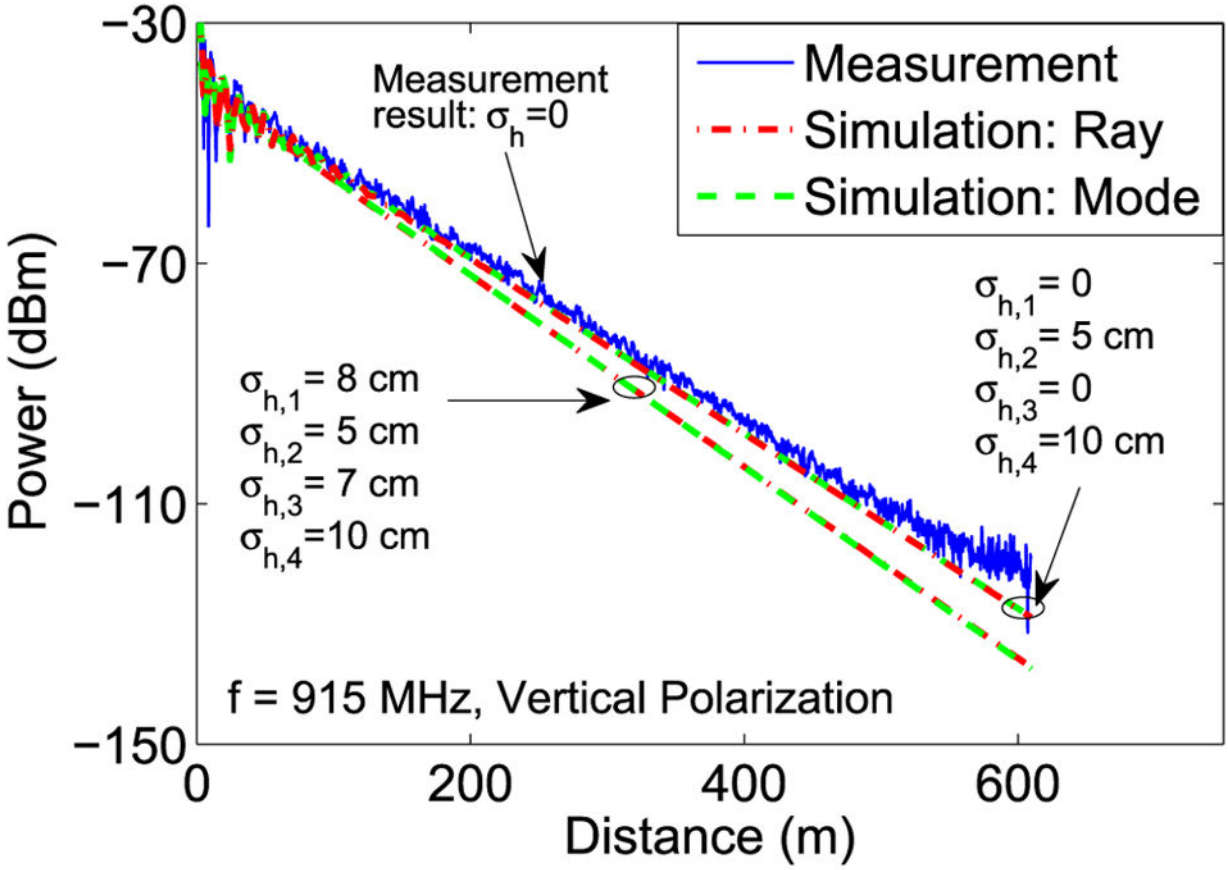

Fig. 7.
Power attenuation in a tunnel with different surface roughnesses on different walls.

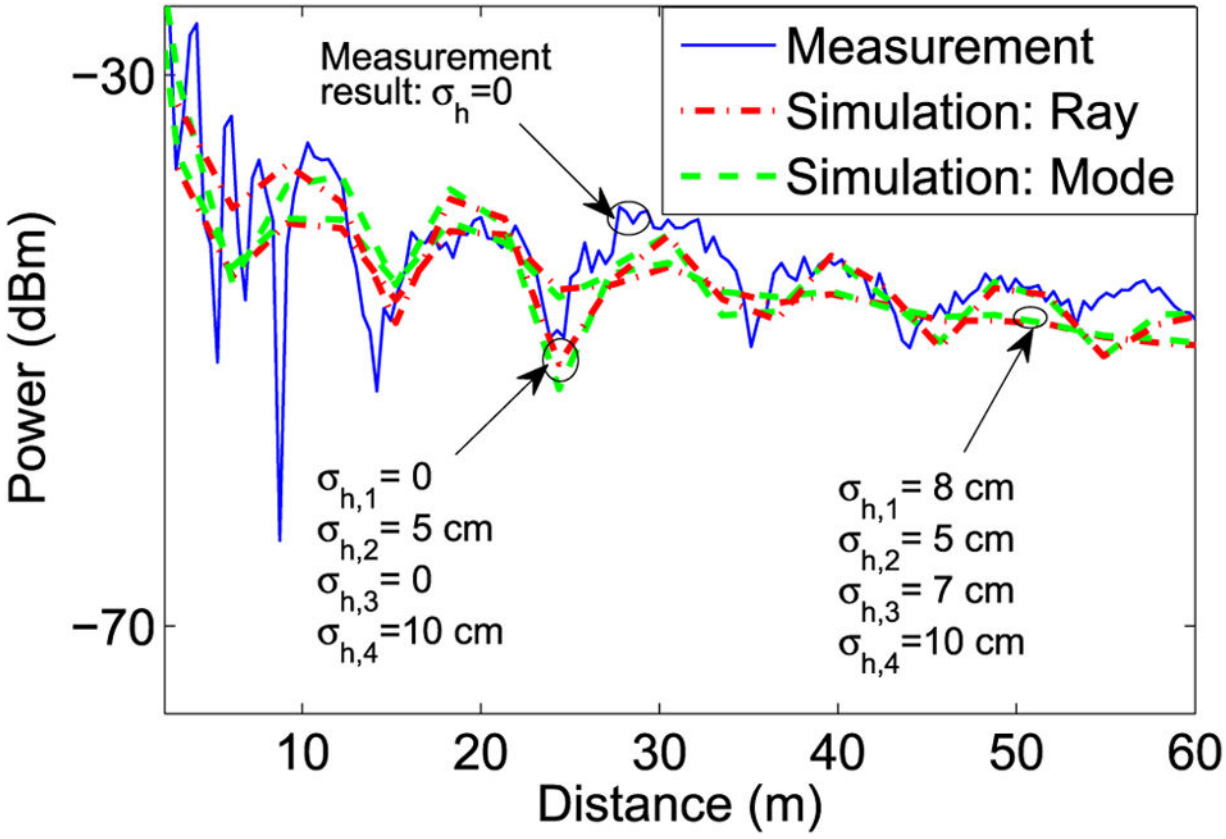

Fig. 8.
Closer view of the first 60-m data in Fig. 7.

TABLE I

Parameters Table

Dimension	Axis	Size	Permitivity	Image	Mode
Horizontal	x	a	ε_a	m	p
Vertical	y	b	ε_b	n	q

TABLE II

Summary of Parameters Used in the Simulation

Parameter	Value	Parameter	Value
Tunnel width (2a)	1.83 m	Re $\{\bar{\varepsilon}_{a,b}\}$	8.9
Tunnel height (2b)	2.35 m	$\sigma_{a,b}$	0.15 S/m
Transmitter height	1.22 m	f	0.45, 0.915 GHz
Receiver height	1.22 m		2.45 GHz

TABLE III

List of Variables

l	m	n	$\bar{x}_1$	$\bar{x}_1$	$\bar{y}_1$	$\bar{y}_1$
1	$2s_1$	$2s_2$	$x_0 - x$	$x_0 - x$	$y_0 - y$	$y_0 - y$
2	$2s_1$	$2s_2 + 1$	$x_0 - x$	$x_0 - x$	$2b - y_0 - y$	$-y_0 - y$
3	$2s_1 + 1$	$2s_2 + 1$	$2a - x_0 - x$	$-x_0 - x$	$2b - y_0 - y$	$-y_0 - y$
4	$2s_1 + 1$	$2s_2$	$2a - x_0 - x$	$-x_0 - x$	$y_0 - y$	$y_0 - y$